Flow, Turbulence and Combustion
https://doi.org/10.1007/s10494-023-00423-4

RESEARCH

Helical structures in a temporally developing round jet in the developed state

Mamoru Takahashi[1] · Ren Fukui[1] · Koichi Tsujimoto[1] · Toshitake Ando[1] · Toshihiko Shakouchi[1]

Received: 16 September 2022 / Accepted: 17 April 2023

Abstract
Although existing studies have investigated dominant structures in round jets in developed states, the image of the structures still has been unclear because the observations have often been based on velocity correlation measurements from a limited number of measurement points. In this study we analyzed a full spatiotemporal jet data generated by a large-eddy simulation (LES) to detect the dominant structures of a round jet much more clearly than ever. To save computational resources, we simulated a temporally developing round jet with a jet Reynolds number of 70, 000. Because the temporally developing jet field is homogeneous and periodic in both the streamwise and azimuthal directions, we analyzed the flow field using Koopman decomposition (KD). To analyze the huge numerical data of the jet, the data were reduced using temporal proper orthogonal decomposition (POD), and KD was subsequently performed for the POD modes. In the developed state of the round jet, two layers (inner and outer) are formed. In the inner layer, single-helical structures are formed, and it is confirmed that their streamwise wavelength is in good agreement with those in existing spatially developing round jets (Samie et al., J. Fluid Mech. 916:A2, 2021). In the outer layer, we newly find triple-helical structures oriented in the streamwise direction more than the single-helices. Although the energy contained by the triple-helices is smaller than that by the single-helices, they display important contributions to the mean velocity diffusion. Finally, we demonstrate that only five types of helices may approximate the original flow field excellently.

Keywords Temporally developing simulation · Round jet · Koopman decomposition

1 Introduction

Jet flows can be encountered in various engineering situations such as thrusters, mixers, and injectors. The momentum diffusion of jets is associated with these devices, and the diffusion performance is widely believed to be determined by certain dominant structures. Knowledge of the dominant structures of jets is required to improve the performance of

✉ Mamoru Takahashi
takahashi@mach.mie-u.ac.jp

[1] Graduate School of Engineering, Mie University, Tsu, Mie 514-8507, Japan

Published online: 01 May 2023

devices involving jets. The formation of dominant structures depends on how the flow is developed; the flow could be in a developing or transition state (near field, $x/D \lesssim 5$, where D is diameter of the jet exit, and intermediate field, $x/D \lesssim 15$) and in a developed state (far field, $x/D \gtrsim 15$). The structures in a round jet, issuing from a circular nozzle, have been particularly widely studied. In the near field of the round jet, the shear layer formed between the faster jet core and the slower ambient fluid are rolled up, and periodic vortex rings are generated. The vortex rings subsequently break down and generate quasi-streamwise vortices in the intermediate field, which are referred to as rib or braid structures (Yule 1978; Hussain 1986; Liepmann 1991), and produce a three-dimensional turbulent flow field.

Compared with the flow in the developing state, the flow in the developed state is much more complex and turbulent. The structures in the far field of a round jet can be observed by techniques such as conditional sampling, two-point correlation, and dimension reduction of the flow data. These techniques support the idea that some dominant structures exist in the apparently disordered turbulent flow field of the round jet. Many previous studies have argued that the dominant structures of round jets in the far field are helical; however, there are conflicting suggestions regarding whether they are single- or double-helical. Several decades ago, evidence for single-helical structures was based on visualization experiments (Dimotakis et al. 1983) and conditional sampling from velocity measurements at a limited number of points (Tso and Hussain 1989). Subsequently, more resolved multipoint velocity measurements demonstrated the dominance of double-helical structures (Gamard et al. 2002, 2004). In recent times, three-dimensional data of simulated jets became available as well as velocity-correlation data from laboratory experiments. Mullyadzhanov et al. (2018) showed the superiority of the single-helical structures and indicated that the existence of the single-helical structures can no longer be dismissed simply owing to insufficient resolution. Samie et al. (2021, 2022) quantified the helical structures in a numerically simulated round jet, which was supported by two-points velocity correlation measurements from a filtered (coarse-grained) velocity singnals.

The above background clearly shows that rich (full spatiotemporal) jet data should be analyzed to acquire detailed images of such dominant structures in a round jet; this is difficult to accomplish by laboratory experiments but relatively easy by numerical simulations. Numerical simulations reproducing the turbulent flows generated in the laboratory using wind tunnels or water channels are referred to as spatially developing simulations. The development of a jet in a spatially developing simulation often suffers from the limitations of numerical setups, such as artificial boundary conditions. The boundaries of the numerical domain must be set sufficiently far from the jet core so that the influence of the artificial boundary condition is sufficiently attenuated; specifically, the outflow boundary should be ideally set at $x/D \sim 100$ considering the location where the fully developed state of the jet is observed. Therefore, the simulation of the far field of a spatially developing jet requires a large computational domain. Furthermore, a long computation time is required for the convergence of the statistics. In this respect, temporally developing simulations of turbulent flows can save computational resources. The temporally developing flow is released in a numerical domain that has a periodic boundary in the streamwise direction (i.e., zero pressure gradient); subsequently, the turbulence grows due to the shear between high- and low-speed flow and subsequently decays owing to energy dissipation. Thus, temporally developing flows acquire streamwise statistical homogeneity at the expense of stationarity. Temporally developing flows have been successfully applied in studies on turbulent shear flow mechanics, for example, studies involving jets as well as shear mixing layers (Rogers and Moser 1994), wakes (Moser et al. 1998), turbulent boundary layers (Watanabe et al.

2019; Kozul et al. 2020), and grid turbulence (Pineau and Bogey 2020). Temporally developing jets have been simulated to study the dynamics near turbulent–non-turbulent interfaces (Silva and Pereira 2008; Taveira and da Silva 2013; van Reeuwijk and Holzner 2014; Nagata et al. 2018; Hayashi et al. 2021), jet noise (Watanabe and Nagata 2018; Bogey and Pineau 2019), and combustion (Hawkes et al. 2012; Yang et al. 2013; Shamooni et al. 2020).

In this study, we aim to detect the dominant structures of the round jet much more clearly than ever, with the aid of numerical data of the round jet obtained by a temporally developing simulation. To realize a high-Reynolds-number setup of the jet and reduce the influence of insufficient spatial resolution, we performed a large-eddy simulation (LES) of the temporally developing round jet. This is easily justified because we are interested in relatively larger-structures than smaller-scale eddies. As the temporally developing round jet is periodic in both the streamwise and azimuthal directions, the flow field is expected to decompose into spatially oscillating modes. Therefore, in this study, Koopman decomposition (KD) is utilized owing to its effectiveness in extracting dominant oscillating structures from numerical data. Since the pioneering introduction to fluid data analysis by Schmid (2010) (referred to as dynamic mode decomposition (DMD) (see also his review (Schmid 2022)), KD has been widely applied to turbulence structure analysis.

The remainder of this paper is organized as follows. Section 2 describes our numerical details and fundamental characteristics of the round jet. Section 3 presents an analysis of the dominant structures of the round jet by means of modal decomposition. Finally, our conclusions are presented in Sect. 4.

2 Numerical details and fundamental characteristics of round jet

2.1 Numerical setup

Figure 1 shows the numerical domains of our jet simulations. In this study, both Cartesian cylindrical coordinate systems were employed. In a Cartesian system, the streamwise direction (velocity) is x (u), the cross-streamwise is y (v), and the spanwise is z (w). In a cylindrical system, the streamwise direction (velocity) is again x (u), but the radial r

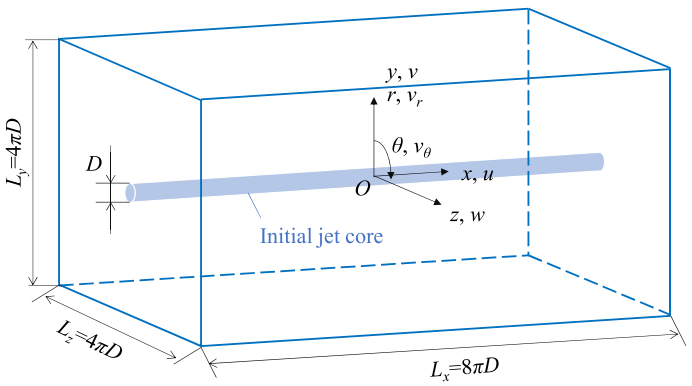

Fig. 1 Schematic of numerical domain and initial jet core

($v_r \equiv \boldsymbol{v}^{\perp} \cdot \boldsymbol{r}/|\boldsymbol{r}|$, where $\boldsymbol{v}^{\perp} \equiv (v, w)$ and $\boldsymbol{r} \equiv (y, z)$), and the azimuthal θ ($v_\theta \equiv \boldsymbol{v}^{\perp} \cdot \boldsymbol{n}$, where $\boldsymbol{n}$ is the unit vector perpendicular to both $\boldsymbol{x}$ and $\boldsymbol{r}$).

The simulation of a temporally developing jet can be achieved using the numerical domain whose boundary in the streamwise direction is periodic. One can choose either periodic or solid wall conditions for vertical boundaries. The former method was employed herein. The numerical domain sizes along the x, y, and z directions were $(L_x, L_y, L_z) = (8\pi D, 4\pi D, 4\pi D)$. The number of grid points is $(N_x, N_y, N_z) = (512, 256, 256)$. If we transform the coordinates into cylindrical ones, $(N_x, N_r, N_\theta) = (512, 128, 256)$ (the flow fields only in $0 < r \leq 2D$ are analyzed). In the initial state, a column-like high-speed region is embedded in the numerical domain.

$$u(y, z) = \begin{cases} U_J & (r \leq D/2), \\ 0 & (r > D/2). \end{cases} \tag{1}$$

The initial jet Reynolds numbers Re_J were $DU_J/\nu = 10,000$, 40, 000, and 70, 000, where ν is the kinematic viscosity of the fluid. All three components in the initial state were disturbed by uniformly distributed random numbers with a root-mean-square value of $0.01U_J$. The simulation time was $0 \leq t^* \equiv tU_J/D \leq 25$, and the time increment Δt was set to 0.01 such that the Courant–Friedrichs–Lewy condition $U_J \Delta t < \Delta x$ ($\equiv L_x/N_x$) was satisfied. The instantaneous, three-dimensional flow data were recorded for the storage of our computer every $10\Delta t$; therefore, we obtained 250 datasets.The numerical code was based on `DNSLab` (Vuorinen and Keskinen 2016), a Navier–Stokes solver that consists of pseudospectral scripts for spatial numerical derivatives, a fourth-order Runge–Kutta scheme for temporal increments, and de-aliasing using the 2/3 rule. Although the original code was written for a two-dimensional flow in a periodic square, it can easily be modified for a three-dimensional flow in a periodic cube. Furthermore, we added the subgrid scale (SGS) stress model for the LES simulation. The governing equations are the Navier–Stokes equations and the continuity equation for the grid-scale (filtered) velocity field $\overline{u_i}$:

$$\frac{\partial \overline{u_i}}{\partial t} + \overline{u_j}\frac{\partial \overline{u_i}}{\partial x_j} = -\frac{\partial \overline{p}}{\partial x_i} + \frac{1}{\nu}\frac{\partial^2 \overline{u_i}}{\partial x_j \partial x_j} - \frac{\partial \tau_{ij}}{\partial x_j}, \tag{2}$$

$$\frac{\partial \overline{u_j}}{\partial x_j} = 0, \tag{3}$$

where p is the static pressure per unit mass, and $\tau_{ij} \equiv \overline{u_i u_j} - \overline{u_i}\,\overline{u_j}$ is the SGS stress. The latter is modeled in the present LES using the Smagorinsky model, which yields

$$\tau_{ij} = -2C\overline{\Delta}^2 \sqrt{2\overline{S_{kl}}\,\overline{S_{kl}}}\,\overline{S_{ij}}, \tag{4}$$

where $\overline{\Delta}$ is the filter width (equivalent to the grid space, which is uniform in this study), $S_{ij} = (1/2)(\partial u_i/\partial x_j + \partial u_j/\partial x_i)$ is the rate-of-strain tensor. Conventionally, the model coefficient C is set to 0.2; however, the value must be modified according to the studied flows. Dynamic Smagorinsky model proposed by Germano et al. (1991) determines the value dynamically using the grid-scale fields, but this may sometimes results in negative (unstable) diffusion; thus, averaging the model coefficient is required. To address these issues, we employed a novel technique by Kobayashi (2005) that proposed the determination of model coefficient C based on the detection of relatively small-scale eddies.

$$C = \frac{1}{20}|F|^{3/2}, \tag{5}$$

where

$$F \equiv \frac{Q}{E}, \tag{6}$$

$$Q = \frac{1}{2}\left(\overline{W_{ij}}\,\overline{W_{ij}} - \overline{S_{ij}}\,\overline{S_{ij}}\right), \tag{7}$$

$$E = \frac{1}{2}\left(\overline{W_{ij}}\,\overline{W_{ij}} + \overline{S_{ij}}\,\overline{S_{ij}}\right), \tag{8}$$

and $W_{ij} = (1/2)(\partial u_i/\partial u_j - \partial u_j/\partial u_i)$ is the rate-of-rotation tensor.

2.1 Fundamental characteristics

In the following, the filtered velocity $\overline{u}$ is simply denoted as u, unless otherwise noted. As the jet flows are statistically unsteady processes, we employ the spatial average in two homogeneous directions (streamwise and azimuthal). For example, the Reynolds decomposition of the instantaneous velocity u is given by

$$u = U + u', \quad U = \langle u \rangle = \frac{1}{8\pi}\frac{1}{2\pi}\int_{-4\pi}^{4\pi}\int_{-\pi}^{\pi} u\mathrm{d}x\mathrm{d}\theta. \tag{9}$$

The diffusion performance of the round jet is characterized by the development of the mean streamwise velocity along the centerline U_C and the half-width of radial distribution of the mean streamwise velocity $r_{0.5}$, as summarized in Fig. 2. To validate our simulation, additional simulations at different Re_Js (40, 000 and 10, 000) were conducted, and compared with each other. At $t^* \lesssim 5$, the round jet contains the potential core, which is indicated as

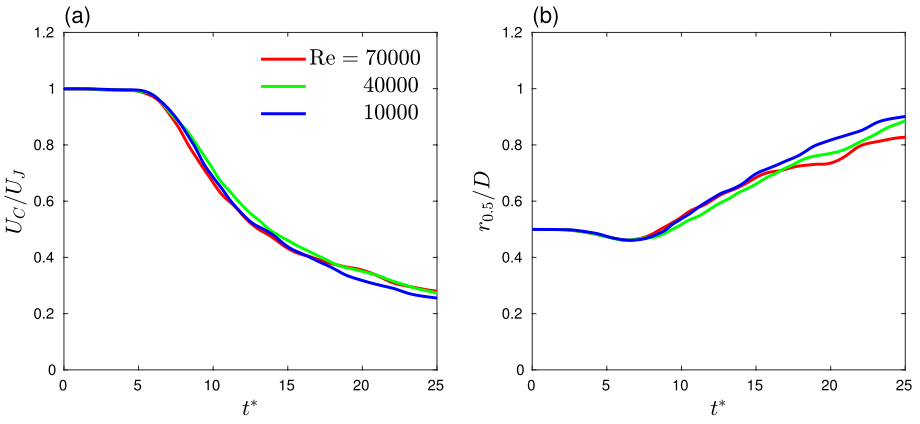

Fig. 2 Temporal variation of mean streamwise velocity along centerline U_C **a** and half-width of radial distribution of mean streamwise velocity $r_{0.5}$ **b**

the unity-normalized mean streamwise velocity, and subsequently the velocity decays. The experimental results in Darisse et al. (2013) demonstrate that U_C/U_J are approximately 0.5 and 0.3 at $x/D = 15$ and 25, respectively, which corresponds well to both $t^* = 15$ and 25 for the current jet. Therefore, t^* can be roughly mapped to x/D locations of the jets in laboratory experiments, despite the difference in their development processes (spatially or temporally developing).

It can also be seen that the results in Fig. 2 are almost independent of the Reynolds number. As the extent of the numerical domain was the same for all three cases, the sizes of the largest eddies in each of the three simulation cases were the same. On the contrary, the size of the smallest eddy decreases at higher Reynolds numbers, but this is not simulated but modeled in the current LESs. Therefore, the above consistency indicates the confidence of our LES technique, even for the largest Reynolds number setup of 70, 000. As we confirmed that the statistical characteristics of the simulated jet are independent of the Reynolds number, we investigated the case with the largest Reynolds number (70, 000) as a representation. We can observe a slight difference in $r_{0.5}/D$ with the Reynolds number. However, this is consistent with experimental evidence showing that jet diffusion decreases with increasing Reynolds number Deo (2005). When the Reynolds number is increased, more small-scale eddies are developed, and more energy is taken away from the large-scale structures. This is the mechanism of the smaller diffusion of the higher Reynolds number jets. It is considered that the present SGS stress model numerically reproduced this phenomenon. Although not displayed here, this Reynolds number dependence was also observed in another trial of simulations. We also found the slight decrease of $r_{0.5}/D$ in $5 \leq t^* \leq 10$, but we could not reveal the mechanism. We consider this is owing to the temporally developing setup, but we do not have enough decision materials at present.

Figure 3 shows the development of the radial distribution of the mean streamwise velocity U, the root mean square of the fluctuating velocity $u^{(rms)} \equiv \sqrt{\langle u'^2 \rangle}$ and $v_r^{(rms)} \equiv \sqrt{\langle v_r'^2 \rangle}$, and the radial Reynolds shear stress $\langle u' v_r' \rangle$. They are normalized by the local characteristics scales U_C and $r_{0.5}$ and are evaluated to check how the flow fields are developed. It is well known that the asymptote of higher-order moments is generally slower than that of lower-order moments. In these results, the distributions of the second-moment statistics for $15 \leq t^*$ are almost self-similar. Based on the above findings, we herein defined the developed state of the simulated round jet as $15 \leq t^*$. Furthermore, we confirm that the self-similar distributions do not considerably deviate from those in Darisse et al. (2015), thereby supporting our numerical confidence.

We evaluated auto-correlation function of the in the streamwise direction for further comparison with the existing experimental database. The correlation function is defined using streamwise velocity at two different location x and x' as,

$$R^U(x - x') \equiv \frac{\langle u'(x) u'(x') \rangle}{\langle u'(x)^2 \rangle}, \tag{10}$$

note that the prime of x' does not indicate the root mean square calculation. Figure 4 is the $R^U(x - x')$ and averaged in $15 \leq t^* \leq 25$ (i.e., we assume similarity of $R^U(x - x')$ in this time interval). The reference data is from a round jet from smooth contraction exit in Xu and Antonia (2002), but the plot is regenerated by ourselves for the present form. The measurement location of the reference data is at 20 diameter downstream from the jet exit. Both the present and reference auto-correlation functions are evaluated at $r/r_{0.5} = 0.25$. The two plots do not departure with each other, supporting the confidence of the present simulations of the jets.

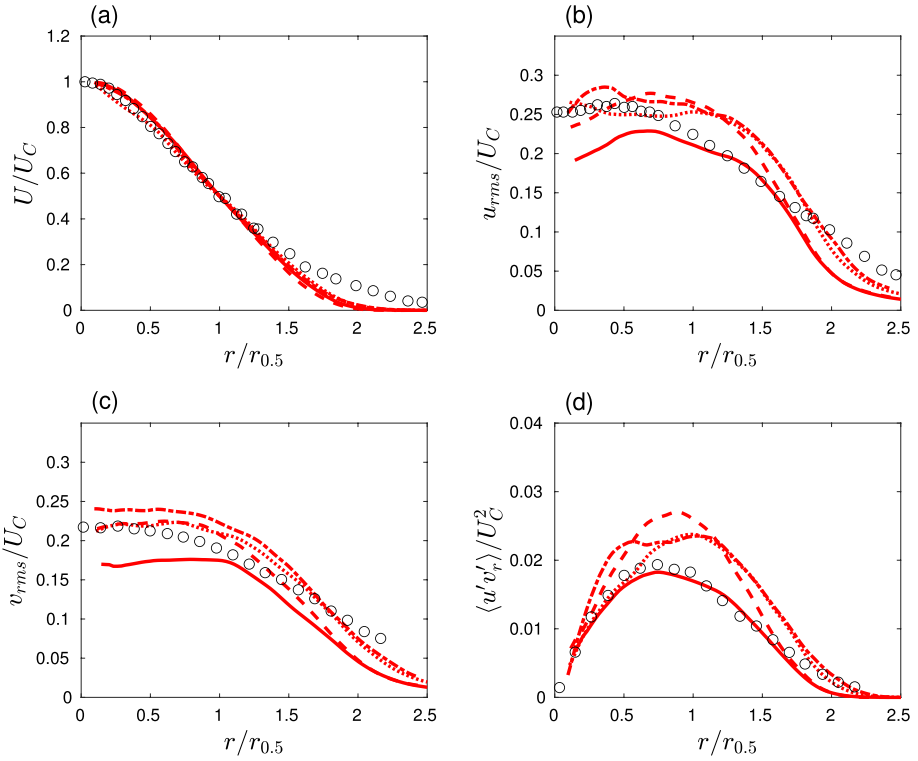

Fig. 3 Temporal variation of mean streamwise velocity U, root-mean-square of fluctuating velocity $u^{(rms)} \equiv \sqrt{\langle u'^2\rangle}$ and $v_r^{(rms)} \equiv \sqrt{\langle v_r'^2\rangle}$, and radial Reynolds shear stress $\langle u'v'_r\rangle$. The Reynolds number is 70, 000. Solid, $t^* = 10$; dashed, 15, dot, 20; dot-dashed, 25. Black open circles are by Darisse et al. (2015)

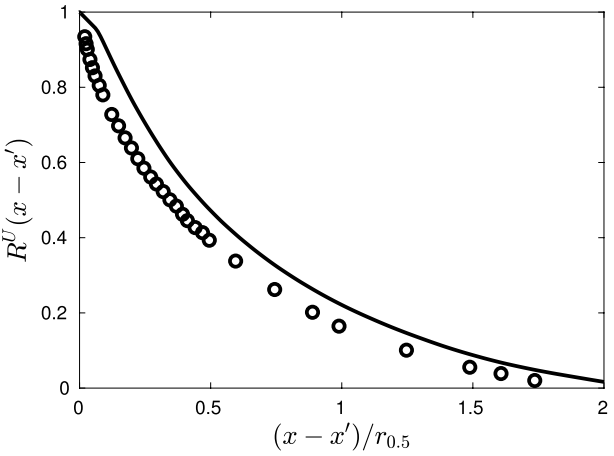

Fig. 4 Auto-correration function of streamwise velocity $R^U(x - x')$ at $r/r_{0.5} = 0.25$. Solid line, present; circle, from Xu and Antonia (2002)

1 Detecting dominant structures using modal analysis techniques

3.1 Data reduction using temporal proper orthogonal decomposition (POD)

To perform KD, all analyzed spatiotemporal flow data must be stored in the memory of the computer. As this step was difficult even for the authors' computer resources, in this study, the data were reduced by POD as a preprocessing step. For the following postprocessing, the flow data at a given time are stacked into column vector $\boldsymbol{u}$. Using the POD, the flow field was approximated using the following equation:

$$\boldsymbol{u}_{Orig}(x, r, \theta, t) \approx \boldsymbol{u}_{POD}(x, r, \theta, t) = \sum_{i}^{r_t} \alpha_i(t)\boldsymbol{\phi}_i(x, r, \theta), \tag{11}$$

where mode $\boldsymbol{\phi}_i$ is the ith eigenvector of the covariance matrix of $\boldsymbol{u}$ ordered by the eigenvalues, and the temporal expansion coefficient α_i can be calculated by projecting $\boldsymbol{u}$ onto $\boldsymbol{\phi}_i$. The standard POD algorithm still requires that all data be stored in memory, which can be avoided using an online (incremental) POD algorithm (Ohmichi 2017; Cardot and Degras 2018). The order of the memory requirements is then reduced to $(2r_t + 1)/Nt$. r_t is 21 herein, as determined from our computational resources. One of the 21 POD modes is the conveniently evaluated time-averaged flow field, that is, $(1/N_t)\sum_n^{N_t} \boldsymbol{u}|_{t=10(n-1)\Delta t}$, where the corresponding temporal expansion coefficient is unity.

The output modes comprise the orthogonal basis of the covariance matrix of $\boldsymbol{u}$, and the variance is evaluated using a time-averaging operation of a statistically unsteady process of a temporally developing flow. Therefore, expecting to obtain any physical insight into the POD modes is difficult. When POD is performed, some of the dominant low-order modes contain cylindrical velocity distributions corresponding to the potential core, which are required to reproduce the near field. As the modes are time-independent, that is, $\boldsymbol{\phi}_i$s are functions of the physical space (x, r, θ), even the intermediate and far fields, where the potential core should have disappeared, are unreasonably reproduced with such components. This is why the reproduction rate tended to decrease later.

As the KD described in the following subsection is multidimensional, one may choose KD for temporal expansion in parallel with the spatial oscillation analysis. In this study, however, the role of modal decomposition is clearly different in space and time; KD is performed for dominant structure extraction, whereas POD is performed purely for data reduction. We are interested in the spatial oscillation of the flow fields rather than the temporal oscillation, and the calculated modes do not need to correspond to temporal sinusoids. Furthermore, as POD modes are the most efficient energy-based results, POD is more suitable than KD for the present objective.

The POD flow field $\boldsymbol{u}_{POD}$ that conserves the original flow field $\boldsymbol{u}_{Orig}$ is evaluated by the fraction of the squared norms of these vectors. Figure 5 shows the temporal variation in $|\boldsymbol{u}_{POD}|/|\boldsymbol{u}_{Orig}|$ for the round jet. In the initial state, the POD flow field $\boldsymbol{u}_{POD}$ reproduced most of the original flow field $\boldsymbol{u}_{Orig}$. Over time, the accuracy of the approximation worsens, but the worst value is 61%. This is improved to 65% if we let $r_t = 41$, but performing KD of the 41 POD modes is difficult. We confirmed that POD preprocessing reasonably reduced the input data for subsequent KD analysis.

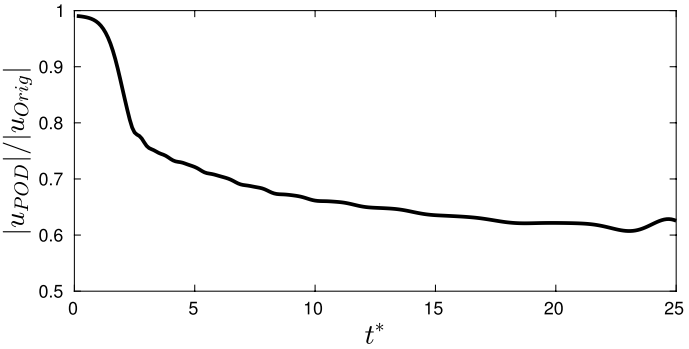

Fig. 5 Temporal variation of squared norm fraction $|\boldsymbol{u}_{POD}|/|\boldsymbol{u}_{Orig}|$

3.2 Analysis of spatial oscillations using Koopman decomposition

3.2.1 Detection of dominant components

Readers can find well-documented KD (or DMD) algorithms in numerous studies such as Schmid (2010); Krake et al. (2021). In this section, we provide a brief description. As a consequence of a typical one-dimensional KD, the original input data are approximately represented by a superposition of modes with sinusoidal oscillation in the specified x direction, that is,

$$\boldsymbol{u} \approx \sum_i a_i \boldsymbol{\varphi}_i \mathrm{e}^{\lambda_i x}, \tag{12}$$

where triplets a_i, $\boldsymbol{\varphi}_i$, and λ_i denote the Koopman amplitudes, modes, and eigenvalues, respectively.

Now, we have $r_t = 21$ POD modes that contain three-dimensional spatial flow information. Therefore, we analyzed all POD modes using KD and again superposed them and then obtained the KD flow field containing a limited number of oscillating modes. We analyzed the oscillations in the streamwise direction x,

$$\boldsymbol{\phi}_i(x, r, \theta) \approx \sum_j^{r_x} a_{ij}^{(x)} \boldsymbol{\varphi}_{ij}^{(x)}(r, \theta) \mathrm{e}^{\lambda_j^{(x)} x}, \quad j = 0, \pm 1, \pm 2 \cdots. \tag{13}$$

These r_x modes are filtered components through low-rank approximation in the singular value decomposition (SVD) process of the KD algorithm, which is essentially equivalent to dimensionality reduction by POD. Owing to the spatial periodicity of the data, the absolute values of the eigenvalues $\lambda_j^{(x)}$ are ideally one, and the wavenumbers $\arg\lambda_j^{(x)}/(8\pi)$ are integers. Thus, hereafter, $\arg\lambda_j^{(x)}/(8\pi) = \pm j$ is referred to as j components or the jth streamwise harmonic in short. The growth/decay of each mode, which is one of the pieces of information contained in the eigenvalues, is trivial herein, and only the other mode (wavenumber or scale) is relevant for discussion. In practice, exact integer values cannot be obtained owing to the numerical errors and POD that provide no information about the periodicity of the data; therefore, the output wavenumbers are rounded to integers and classified as their respective harmonics. If the input data are periodic, KD is equivalent to a discrete Fourier transform (DFT) (Rowley et al. 2009). Our analysis essentially comprises bandpass

filtering of the flow data along the streamwise and azimuthal wavenumbers. However, using DFT, obtaining smooth filtered data that contain only a few oscillating modes is difficult, owing to the Gibbs phenomenon. Furthermore, the KD algorithm includes singular value decomposition (SVD), which is equivalent to POD and provides an objective dimension reduction.

Using the periodicity of the data, it is widely known that POD modes are reduced to Fourier modes (Sirovich 1987). Therefore, one can again employ POD in x as well as t. However, we employ DK because it explicitly outputs the oscillating wavenumbers corresponding to KD modes, which is important for our discussion. The other possibilities of modal decomposition techniques are Fourier mode decomposition (FMD, note that this is distinguished from DFT) or spectral POD (SPOD). FMD is applied in Ma et al. (2015) because of its performance of reducing both the calculating difficulty and time consumption. In Towne et al. (2018), SPOD is compared with DMD. They demonstrated that SPOD modes are also DMD modes for homogeneous data. Both two studies did not point out any crucial defect of KD, and thus the applicability of FMD and SPOD does not deny the adequacy of the present technique.

Consequently, the flow field consisting of dominant oscillating motions at a given time is determined as follows:

$$\boldsymbol{u}_{Orig}(x,r,\theta,t) \approx \boldsymbol{u}_{KDx}(x,r,\theta,t) = \sum_{i}^{r_t}\sum_{j}^{r_x} \alpha_i(t) a_{ij}^{(x)} \boldsymbol{\varphi}_{ij}^{(x)}(r,\theta) \mathrm{e}^{\lambda_j^{(x)} x}. \tag{14}$$

Since the data is also periodic along the azimuthal direction θ, the oscillation in the θ can be analyzed as well as x,

$$\boldsymbol{\phi}_i(x,r,\theta) \approx \sum_{k}^{r_\theta} a_{ik}^{(\theta)} \boldsymbol{\varphi}_{ik}^{(\theta)}(r,x) \mathrm{e}^{\lambda_k^{(\theta)}\theta}, \quad k = 0, \pm 1, \pm 2 \cdots \tag{15}$$

which is considered in this subsection together with Eq. (13). The reconstructed flow field is also given as,

$$\boldsymbol{u}_{Orig}(x,r,\theta,t) \approx \boldsymbol{u}_{KD\theta}(x,r,\theta,t) = \sum_{i}^{r_t}\sum_{k}^{r_\theta} \alpha_i(t) a_{ik}^{(\theta)} \boldsymbol{\varphi}_{ik}^{(\theta)}(r,x) \mathrm{e}^{\lambda_k^{(\theta)}\theta}. \tag{16}$$

Then, of course, the absolute values of eigenvalues $\lambda_k^{(\theta)}$ are ideally one and the wavenumbers $\arg\lambda_k^{(\theta)}/(2\pi)$ are integers, and $\arg\lambda_k^{(\theta)}/(2\pi) = \pm k$ is referred to as k components or the sth azimuthal harmonic.

We considered the relative importance of each harmonic component. Conventionally, the triplet output by KD has been individually evaluated, but Krake et al. (2021) criticized this approach and recommended considering alternative quantities obtained by combining several of them. Here, we consider *scaled modes* $a_{ij}^{(x)}\boldsymbol{\varphi}_{ij}^{(x)}$ or $a_{ik}^{(\theta)}\boldsymbol{\varphi}_{ik}^{(\theta)}$, that is, the mode that considers amplification by the coefficient. The relative importance of each harmonic component is then evaluated by the norm resulting from taking the scaled modes corresponding to the wavenumber from all the POD modes and superposing them.

$$Norm_{KDx}^{(j)} \equiv \left| \sum_{i} \alpha_i a_{ij}^{(x)} \boldsymbol{\varphi}_{ij}^{(x)} \right|, \tag{17}$$

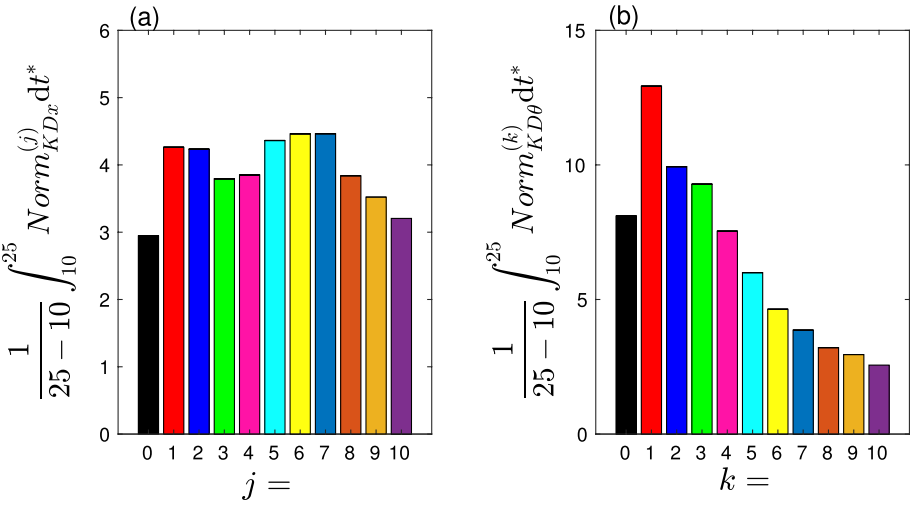

Fig. 6 **a** $Norm_{KDx}^{(\kappa_j^{(x)})}$ and **b** $Norm_{KD\theta}^{(\kappa_k^{(\theta)})}$ averaged in $10 \le t^* \le 25$

$$Norm_{KD\theta}^{(k)} \equiv \left| \sum_i \alpha_i a_{ik}^{(\theta)} \boldsymbol{\varphi}_{ik}^{(\theta)} \right|. \tag{18}$$

The time-averaged $Norm_{KDx}^{(j)}$ and $Norm_{KD\theta}^{(k)}$, up to the 10th harmonics, are plotted in Fig. 6a and b, respectively. All bars plotted in Fig. 6a are almost the same height with each other, indicating the difficulty of the selection of the dominant components from this graph. On the other hand, obviously, the bars in Fig. 6b is almost ordered according to the azimuthal oscillating wavenumbers. The most dominant component is $k = 1$ followed by $k = 2$ as well as 3. The $k = 0$ components, namely axisymmetric component, is not so outstanding in the present flow field. From this result, it is reasonable for us to promote the following discussions focusing on the results of the KD in the azimuthal direction, rather than the streamwise direction.

Next, we evaluated the contribution of each Koopman mode to the Reynolds shear stress, which is given by

$$\langle u' v'_r \rangle_{KD\theta} = \frac{1}{4\pi} \frac{1}{2\pi} \int_{-2\pi}^{2\pi} \int_{-\pi}^{\pi} u'_{KD\theta} v'_{r,KD\theta} \mathrm{d}x \mathrm{d}\theta. \tag{19}$$

The KD fluctuating velocity component $u'^{(k)}_{KD\theta}$ is denoted by $u'^{(k)} \mathrm{e}^{i\kappa_k^{(\theta)}\theta}$. Subsequently, the cross components $u'^{(k_1)} v'^{(k_2)}_r \mathrm{e}^{i\kappa_{k_1}^{(\theta)}\theta} \mathrm{e}^{i\kappa_{k_2}^{(\theta)}\theta}$ $(k_1 \neq k_2)$ appear, but they vanish owing to the orthogonality of the complex exponential functions, that is,

$$u'^{(k_1)} v'^{(k_2)}_r \int_{-2\pi}^{2\pi} \mathrm{e}^{i\kappa_{k_1}^{(\theta)}\theta} \mathrm{e}^{i\kappa_{k_2}^{(\theta)}\theta} \mathrm{d}\theta = 0. \tag{20}$$

Therefore, the Reynolds shear stress of the KD flow field $\overline{uv_r}_{KD}$ is equal to the sum of the Reynolds shear stresses of each Koopman mode as follows:

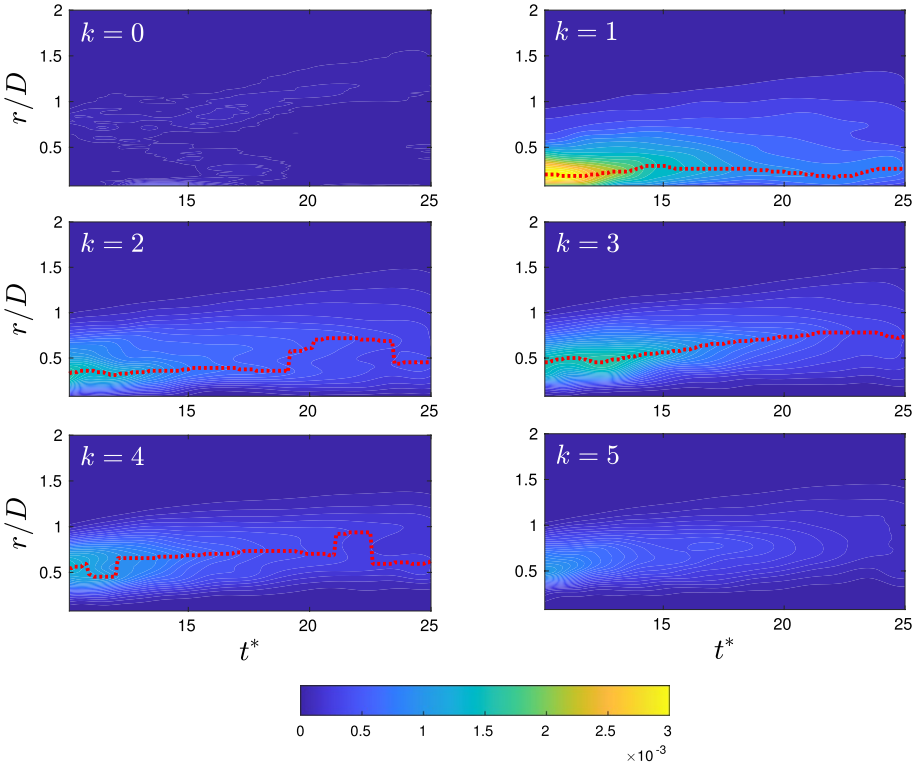

Fig. 7 Temporal variation of Reynolds shear stress $\langle u'v'_r \rangle$ due to the 0th, 1st, .., and 5th azimuthal harmonics in $10 \leq t^* \leq 25$

$$\langle u'v'_r \rangle_{KD\theta} = \langle u'v'_r \rangle_{KD\theta}^{(k=1)} + \langle u'v'_r \rangle_{KD\theta}^{(k=2)} + \cdots . \tag{21}$$

Therefore, we can separately evaluate the momentum diffusion performance of each Koopman mode.

Figure 7 illustrates the temporal variation of the radial distribution of the Reynolds shear stress contributed by the 0th, 1st, .., and 5th azimuthal harmonics in $10 \leq t^* \leq 25$. The components showing the largest Reynolds shear stress is the 1st harmonic, followed by the 2nd, 3rd, and 4th, which is the same as we have just seen in Fig. 6b. The 0th harmonic (axisymmetric component) contributes to the momentum diffusion much lesser than the above dominant components. The Reynolds shear stress due to the higher kth harmonics are not illustrated, but we have confirmed that they also do not show large Reynolds shear stress.

Furthermore, temporal variation of the r/D location, at which the Reynolds shear stress due to each of the 1s, 2nd, 3rd, and 4th harmonic is maximum, is plotted by the red-doted line. Interestingly, While the peaks of the Reynolds shear stress due to the 1st and 2nd harmonics are near the centerline ($r/D \lesssim 0.5$), those due to the 3rd and 4th harmonics are located relatively outer ($r/D \gtrsim 0.5$). This implies the multi-layer structure of the present round jet field. Several points where the lines sharply break are observed in the plots of the 2nd and 4th harmonics. This is caused by the increase or decrease of the maximum

value of the Reynolds shear stress. It is considered that each of the kth harmonic itself consists of several structures layered in the radial direction. For example, the most dominant structure in the 2nd harmonic is in the inner layer ($r/D \lesssim 0.5$), but which is weakened in $15 \leq t^* \leq 20$. Consequently, the structure in the outer layer ($r/D \gtrsim 0.5$) is temporally dominant in $19 \leq t^* \leq 24$.

To the authors' knowledge, such a multi-layered feature of the dominant structures of turbulent round jet flows has not been reported by the existing studies. In many studies, the dominance of the structures has been often evaluated only by the energy carried by the structures. Of course, this is quite natural and not criticized, given that the discussions on the large-scale structures have been driven by the energy-based techniques such as POD. The Reynolds shear stress in Fig. 7, on the other hand, is also an important quantity as well as the energy from the engineering viewpoint. However, not only that, it may provide such useful information on the radial distribution of the large-scale structures.

3.3 Visualization of dominant structures

From the above results, we attempt to visualize the dominant structures in the innner and oute layer separately. The most dominant azimuthal oscillating component is the 1st harmonics in the inner layer while the 3rd harmonics in the outer later. Now, the components oscillating at the given azimuthal wavenumbers are detected by the current scheme of POD and KD in azimuthal direction. The dominant $k = 1$ and 3 components are further analyzed, while $k = 2$ and 4 are not, since their contributions (in terms of both squared norm and Reynolds shear stress) are not prior in the inner and outer layer, respectively.

The 1st and 3rd azimuthal harmonics are again Koopman decomposed in the streamwise direction,

$$\begin{aligned} \boldsymbol{u}^{(k)}_{KD\theta}(x,r,\theta,t) &= \sum_{i}^{r_t} \alpha_i(t) a^{(\theta)}_{ik} \boldsymbol{\varphi}^{(\theta)}_{ik}(r,x) \mathrm{e}^{\lambda^{(\theta)}_k \theta} \\ &\approx \sum_{l}^{r_x} a^{\prime(x)}_{l}(t) \boldsymbol{\varphi}^{\prime(x)}_{l}(r,\theta,t) \mathrm{e}^{\lambda^{(x)}_l x}. \end{aligned} \tag{22}$$

Numbers of existing studies (Dimotakis et al. 1983; Tso and Hussain 1989; Gamard et al. 2002, 2004; Mullyadzhanov et al. 2018; Samie et al. 2021, 2022) have suggested that large-scale structures in round jets consist of certain helical structures. If such helical structures are also present in the current round jet, the streamwise KD may clarify the helicity of the structures. We have performed temporal POD and azimuthal KD, and many of the components have been truncated, although our analysis has been conducted to preserve the dominant structures. If the preserved components are further dimension-reduced by this streamwise oscillation analysis, the momentum exchange performance of the remaining components is evaluated to be quite small. Therefore, the streamwise KD was only applied to classify the helical characteristics of each azimuthal harmonic for distinct visualization.

Since each KD mode $\boldsymbol{\varphi}^{\prime(x)}_{l}(r,\theta,t)$ is normalized so that its squared norm is unity, the amplitude of the harmonic component is characterized by the coefficient $a^{\prime(x)}_{l}(t)$. This is unlike the azimuthal KD because the streamwise KD is not combined with POD As in Eq. (22). $a^{\prime(x)}_{l}$ is a complex variable appearing together with its complex conjugate $a^{\prime(x)*}_{l}$, thus the absolute value of $2\mathrm{Real}(a^{\prime(x)}_{l}) = a^{\prime(x)}_{l} + a^{\prime(x)*}_{l}$ is evaluated. The time averaged $2\mathrm{Real}(a^{\prime(x)}_{l})$ is illustrated in Fig. 8a and b for the 1st and 3rd azimuthal harmonics, respectively. In Fig. 8a, the largest $2\mathrm{Real}(a^{\prime(x)}_{l})$ is displayed by $l = 7$, namely the tth streamwise harmonic,

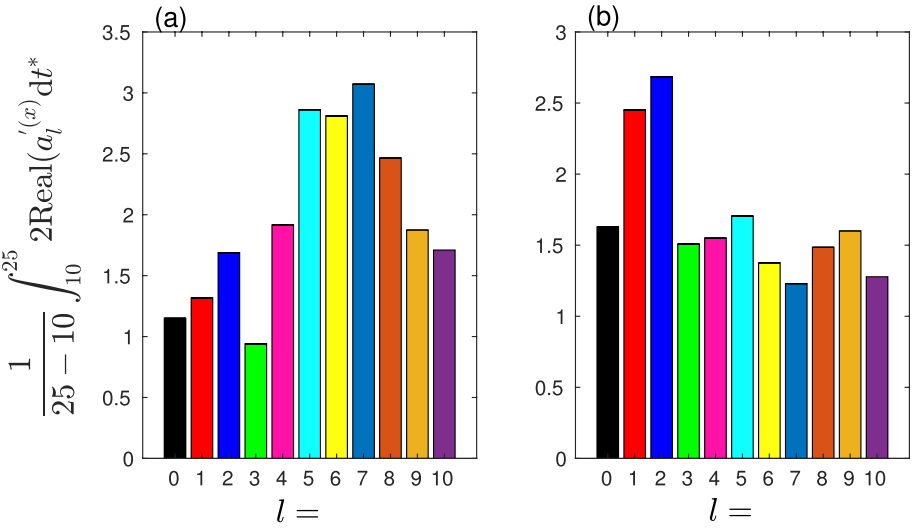

Fig. 8 KD coefficient $2\mathrm{Real}a_l^{'(x)}$ for **a** $k = 1$ and **b** $k = 3$ averaged in $10 \leq t^* \leq 25$

followed by the 5th and 6th. One may consider the 9th harmonic also show the large amplitude. In Fig. 8b, the amplitude of $l = 1$ and 2 components, namely the 1st and 2nd streamwise harmonics, are outstanding. From these results, it is expected that the large-scale structure in the current jet is characterized by two helical structures; one is the inner single-helical structure whose streamwise wavenumber is about 6, and the other is the outer triple helical structure which is oriented in the streamwise direction more than the former. It is worth noting that Samie et al. (2021) proposed a criterion of $4r_{0.5}$ that distinguishes the large-scale motions from the smaller eddies. In our simulation, $4r_{0.5}|_{t^*=25} \simeq 3.7 \simeq 1/6.8$; thus, the harmonics of $j \leq 7$ were sorted into large-scale motions, which is in good agreement with the above criterion. Therefore, we believe with high confidence that such large-scale structures observed in the existing studies are also present in the current LES data of temporally developing round jet.

3.3.1 The 1st azimuthal harmonics: single-helices

Figure 9 shows the visualization of the three dominant streamwise oscillations in the 1st azimuthal harmonics, namely $l = 5$, 6, and 7. The flow field only at $t^* = 20$ is used for the illustration, but the temporal variation of the image in $10 \leq t^* \leq 25$ is provided in the Movie 1 in the supplemental materials, which contributes to our discussion. The contours show the streamwise velocity, and the arrangement of slanting stripe over the $x - \theta$ plane indicates the existence of single-helical structures. In Fig. 9, the $l = 6$ component especially shows a clear stripe arrangement. Meanwhile, the arrangements of the $l = 5$ and 7 components over the $x - \theta$ planes in Fig. 9 is rather a checkerboard (anti-symmetric) than a stripe, but this can be formed by the combination with the mirror-symmetric counterpart (see Tso and Hussain (1989); Gamard et al. (2002; 2004); Mullyadzhanov et al. (2018)). The amplitudes of these two-symmetric helices are not always comparable; in the supplemental movie, we can observe several moments where the tilting of the stripe is being altered. The KD outputs the modes according only to the oscillation frequency, and the

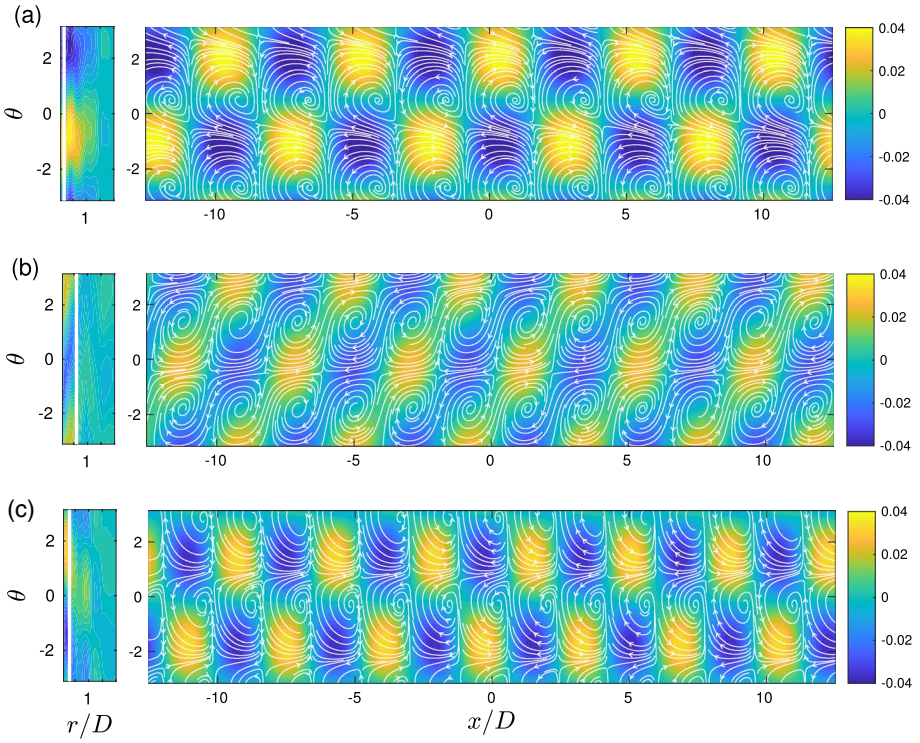

Fig. 9 contour of streamwise velocity in the 1st azimuthal harmonics over $r-\theta$ and $x-\theta$ planes at $t^*=20$. **a** The $l=5$, **b** 6, and **c** 7 streamwise oscillations. The r locations of the $x-\theta$ planes are selected so that the Reynolds shear stress due to the flow field is the maximum (indicated by the white lines displayed in $r-\theta$ planes). In the visualization over $x-\theta$ planes, planar streamlines (u, v_θ) are illustrated together with the streamwise velocity contours

direction of the helix cannot be distinguished. Incidentally, if one performs POD in x, the two mirror-symmetry helices may be separated.

The single-helices of $l=5$ and 7 streamwise oscillations are located in the inner layer ($r/D \lesssim 0.5$) throughout the time period $10 \le t^* \le 25$, which is as we expected in Fig. 7. Unlike these two components, $l=6$ helices are transported from the inner to the outer layer ($r/D \lesssim 0.5$) as time passes. As confirmed in this visualization, the components consisting of only one azimuthal oscillation even display the multi-layered feature. Consequently, the single-helical structures can be observed in the wide range of r/D although the major part is concentrated in the inner layer.

3.3.2 The 3rd azimuthal harmonics: triple-helices

As well as the 1st harmonic in Fig. 9, the 3rd harmonic is visualized, and of course the temporal variation in $10 \le t^* \le 25$ is also provided in the Movie 2. Figure 10 is the visualization of the two dominant streamwise oscillations in the 3rd azimuthal harmonics, namely $l=1$ and 2. Like the 1st harmonic, these components display the tilted stripes or checkerboard arrangement of streamwise velocity, indicating the triple-helical structures. It is

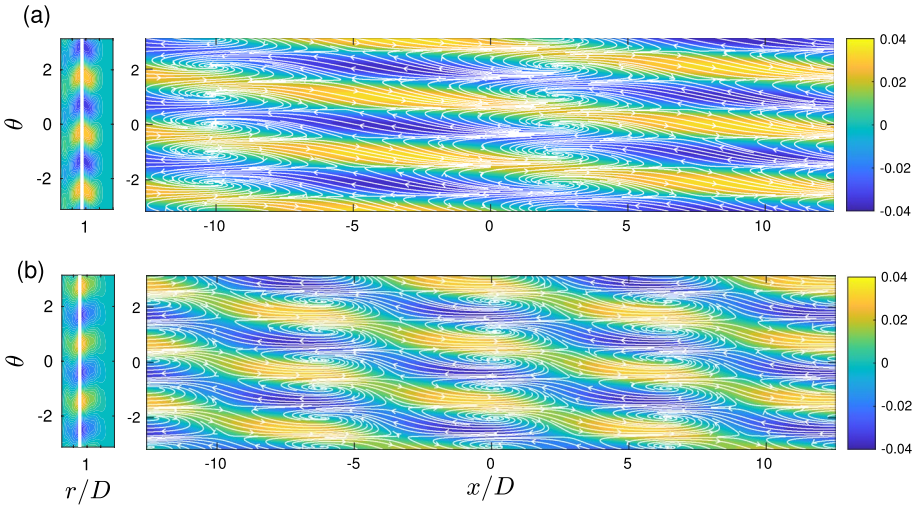

Fig. 10 The same as Fig. 9, but for the 3rd azimuthal harmonics. **a** The 1st and **b** 2nd streamwise oscillations

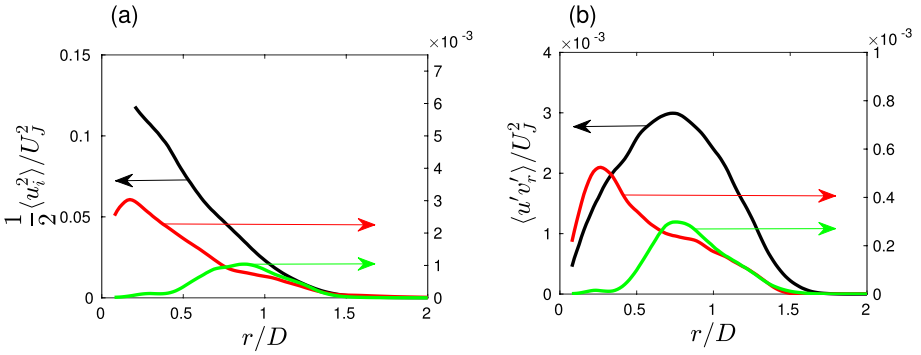

Fig. 11 Radial distribution of **a** turbulent kinetic energy and **b** Reynolds shear stress at $t^* = 20$. Brack solid, from the original flow field; red solid, the 1st azimuthal harmonic; blue solid, the 3rd harmonic; black dashed, sum of the red and blue distributions

consistent with Fig. 7 that these structures tend to be located in $r/D \gtrsim 0.5$, outer than the single-helical structures.

This result implies the existence of very long structures in the round jet, much longer than the single-helices in the inner layer. To the authors' knowledge, such structures have not been reported in the existing studies on round jets. We should require more examination attempting to detect these motions in the spatially developing jets. Note that, however, we found that the distribution of the Reynolds shear stress from the original flow field cannot be explained without these structures. Figure 11 is the Radial distribution of turbulent kinetic energy and Reynolds shear stress from the original flow field, the single-helices, and the triple-helices at $t^* = 20$. Figure 11a shows that the kinetic energy contained by the triple helices (the green line) is obviously smaller than that by the single helices (the red line). Owing to such relatively less energy, it is considered that the triple-helices (or any

other corresponding structures in the outer layer) might have been truncated so far in the modal analysis process. The peak of the turbulent kinetic energy of the single-helices is located at $r/D \sim 0.2$ at this time, and the same is also found in the distribution of Reynolds shear stress. Meanwhile, the peak of turbulent kinetic energy and Reynolds shear stress of the triple-helices at $r/D \sim 0.7$, which is the same as the location where the Reynolds shear stress of the original flow field is the maximum. As already discussed, since the major part of the single-helical structures are in the inner layer although they are distributed wide *r*/*D* range, they do not display so large contributions to the mean velocity diffusion in the outer layer. Instead, this is performed by the relatively minor structures of the triple-helices in the current jet. From these results, at present, the triple-helices cannot be neglected easily as fictitious structures generated by the numerical setup of the spatial periodicity.

3.3.3 Reconstruction using the helical structures and its three-dimensional visualization

Finally, the combination of the five types of helical structures illustrated in Figs. 9 and 10 is examined to confirm to be an approximation of the flow field. Three dimensional illustrations using the iso-surface of fluctuating streamwise velocity u' is shown in Fig. 12 for both the original flow field and the sum of the five dominant helical structures at $t^* = 20$. Despite that the latter consists of only five components which oscillate spatially in sinusoidal waves, it excellently reproduces the rough arrangement of the velocity variation of the original flow field. This is the evidence that our modal analysis captures well the major feature of the input flow field. Such a fully spatiotemporal image of the dominant structures has not ever been provided. Motivated by this result, we expect that the numerical data of

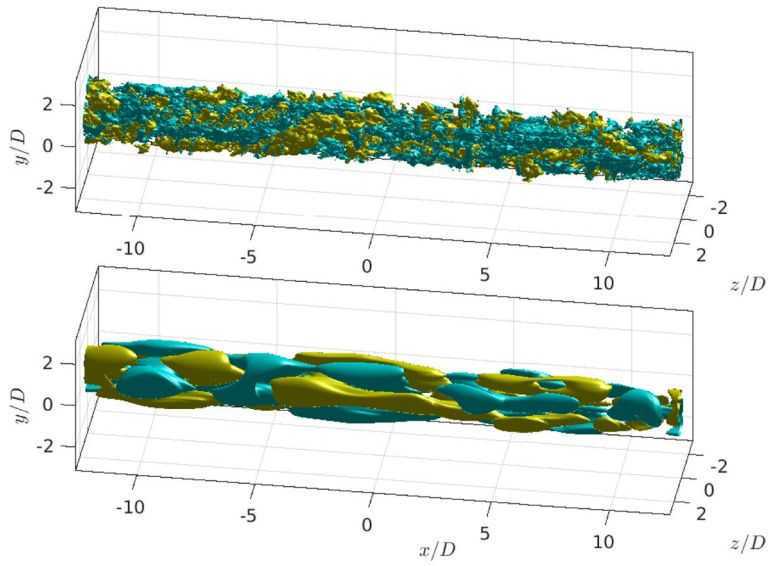

Fig. 12 Iso-surface of fluctuating streamwise velocity u' in (top) the original flow field and (bottom) sum of the five dominant helical structures at $t^* = 20$. The yellow and cyan surface indicate the high and low speed regions, respectively (10% of the maximum and minimum velocity)

the temporally developing flow is more employed for the investigation of large-scale structures in shear turbulence.

2 Conclusion

In this study, we attempted detecting large-scale structures in the numerical data of a round jet with an initial jet Reynolds number of 70, 000. Although numerical simulation data have recently contributed, observations of the large-scale structures of round jets had often been based on the results of measurements that provide limited information, such as two-point correlation measurements. We performed LES of temporally developing round jets, by which we reproduced the fully developed state of round jets using saved computational resources compared to the simulation of a spatially developing jet. The statistical characteristics of the jets are almost independent of the jet Reynolds numbers (however, only a slight decrease in the spread with increasing Reynolds number is observed), which gives confidence to our LES techniques. As the temporally developing round jets are homogeneous in both the streamwise and azimuthal directions instead of being unsteady, the spatial structure of the jet is analyzed using multidimensional KD. Furthermore, we employed POD data reduction before KD so that the extensive spatiotemporal jet data were adequately analyzed using less memory of the computer.

The most dominant structures in the current round jet are single helix structures, which is as proposed in several existing studies. The streamwise wavelength of the detected single-helices are approximately $4r_{0.5}$, which is consistent with the helical structure in Samie et al. (2021). This supports that a numerical data of the turbulent shear flow is useful to investigate the physics of the large-scale structures, even if it is temporally developing flow. Many studies have confirmed that the characteristics of the jet in the developed state depend on the initial (upstream) conditions, such as the turbulence intensity, radial profile of the mean velocity, or even exit geometries (triangle, rectangle, elliptic, among others) (see the review by George (2012)). Some conditions may result in the formation of double-helical structures instead of single-helical structures. It is easy for the current numerical technique to modify the above specific initial conditions; therefore, we hope that this study contributes to determining the jet conditions that can form dominant structures.

Using the full spatiotemporal jet data generated by the numerical simulation, our results provide more detailed images than those of existing studies. The shear layer of the round jet can further split into outer and inner layers. Although the single-helices are observed over the shear layer, the major part is located in the inner layer. In the outer layer, meanwhile, triple-helical structures are found. They are also important for the current round jet in terms of their contributions to mean velocity diffusion, although the contained turbulent kinetic energy is inferior to the single-helices. Using only the single helical structures, the Reynolds shear stress distribution from the original flow field cannot be explained. Finally, the combination of the five types of helical structures (three in the inner and two in the outer layer) is confirmed to be indeed a good approximation of the original flow field, supporting the confidence of the current modal analysis techniques. For further understanding, continuing investigations attempting to detect such very long structures in the outer layer are required.

Supplementary Information The online version contains supplementary material available at https://doi.org/10.1007/s10494-023-00423-4.

Acknowledgements M.T. is grateful for financial support from the Okasan-Kato Foundation, Maeda Engineering Foundation, and the JSPS Grants-in-Aid for Scientific Research (22K14179).

Author contributions MT considered this study and build numerical codes. MT and RF conducted numerical experiments and analyzed the obtained numerical data. All authors contributed equally to discussions to reach our conclusions and reviewed the manuscript.

Funding Okasan-Kato Foundation, Maeda Engineering Foundation, and the JSPS Grants-in-Aid for Scientific Research (22K14179).

Data availability Two movies illustrating the evolution of the dominant structures (Figs. 9 and 10) are supplied as Movie 1 and 2, respectively. The numerical data and simulation scripts can be made available if needed.

Declarations

Conflict of interest The authors declare that they have no conflicts of interest.

Ethical approval Not applicable.

Informed consent Not applicable.

References

Bogey, C., Pineau, P.: Potential-core closing of temporally developing jets at mach numbers between 0.3 and 2: Scaling and conditional averaging of flow and sound fields. Phys Rev Fluids **4**, 124,601 (2019). https://doi.org/10.1103/PhysRevFluids.4.124601

Cardot, H., Degras, D.: Online principal component analysis in high dimension: Which algorithm to choose? Int. Stat. Rev. **86**(1), 29–50 (2018). https://doi.org/10.1111/insr.12220

Darisse, A., Lemay, J., Benaïssa, A.: LDV measurements of well converged third order moments in the far field of a free turbulent round jet. Exp. Thermal Fluid Sci. **44**, 825–833 (2013). https://doi.org/10.1016/j.expthermflusci.2012.09.028

Darisse, A., Lemay, J., Benaïssa, A.: Budgets of turbulent kinetic energy, Reynolds stresses, variance of temperature fluctuations and turbulent heat fluxes in a round jet. J. Fluid Mech. **774**, 95–142 (2015). https://doi.org/10.1017/jfm.2015.245

da Silva, C.B., Pereira, J.C.: Invariants of the velocity-gradient, rate-of-strain, and rate-of-rotation tensors across the turbulent/nonturbulent interface in jets. Phys. Fluids (2008). https://doi.org/10.1063/1.2912513

Deo, R.C.: Experimental Investigations of The Influence of Reynolds Number and Boundary Conditions on a Plane Air Jet. PhD thesis, The University of Adelaide (2005)

Dimotakis, P.E., Miake-Lye, R.C., Papantoniou, D.A.: Structure and dynamics of round turbulent jets. Phys. Fluids **26**(11), 3185–3192 (1983). https://doi.org/10.1063/1.864090

Gamard, S., George, W.K., Jung, D., et al.: Application of a "slice'' proper orthogonal decomposition to the far field of an axisymmetric turbulent jet. Phys. Fluids **14**(7), 2515–2522 (2002). https://doi.org/10.1063/1.1471875

Gamard, S., Jung, D., George, W.K.: Downstream evolution of the most energetic modes in a turbulent axisymmetric jet at high Reynolds number. Part 2. The far-field region. J. Fluid Mech. **514**(May), 205–230 (2004). https://doi.org/10.1017/S0022112004000175

George, W.K.: Asymptotic effect of initial and upstream conditions on turbulence. J. Fluids Eng. **134**(6), 061203 (2012). https://doi.org/10.1115/1.4006561

Germano, M., Piomelli, U., Moin, P., et al.: A dynamic subgrid-scale eddy viscosity model. Phys. Fluids A **3**(7), 1760–1765 (1991). https://doi.org/10.1063/1.857955

Hawkes, E.R., Chatakonda, O., Kolla, H., et al.: A petascale direct numerical simulation study of the modelling of flame wrinkling for large-eddy simulations in intense turbulence. Combust. Flame **159**(8), 2690–2703 (2012). https://doi.org/10.1016/j.combustflame.2011.11.020

Hayashi, M., Watanabe, T., Nagata, K.: The relation between shearing motions and the turbulent/non-turbulent interface in a turbulent planar jet. Phys. Fluids **33**(5), 055,126 (2021). https://doi.org/10.1063/5.0045376

Hussain, A.K.M.F.: Coherent structures and turbulence. J. Fluid Mech. **173**, 303–356 (1986). https://doi.org/10.1017/S0022112086001192

Kobayashi, H.: The subgrid-scale models based on coherent structures for rotating homogeneous turbulence and turbulent channel flow. Phys. Fluids **17**(4), 045,104 (2005). https://doi.org/10.1063/1.1874212

Kozul, M., Hearst, R.J., Monty, J.P., et al.: Response of the temporal turbulent boundary layer to decaying free-stream turbulence. J. Fluid Mech. **896**, A11 (2020). https://doi.org/10.1017/jfm.2020.320

Krake, T., Reinhardt, S., Hlawatsch, M., et al.: Visualization and selection of dynamic mode decomposition components for unsteady flow. Visual Inf. **5**(3), 15–27 (2021). https://doi.org/10.1016/j.visinf.2021.06.003

Liepmann, D.: Streamwise vorticity and entrainment in the near field of a round jet. Phys. Fluids **3**(5), 1179–1185 (1991). https://doi.org/10.1063/1.858046

Ma, L., Feng, L., Pan, C., et al.: Fourier mode decomposition of piv data. SCIENCE CHINA Technol. Sci. **58**(11), 1935–1948 (2015). https://doi.org/10.1007/s11431-015-5908-y

Moser, R.D., Rogers, M.M., Ewing, D.W.: Self-similarity of time-evolving plane wakes. J. Fluid Mech. **367**, 255–289 (1998). https://doi.org/10.1017/S0022112098001426

Mullyadzhanov, R.I., Sandberg, R.D., Abdurakipov, S.S., et al.: Propagating helical waves as a building block of round turbulent jets. Phys Rev Fluids **3**(062), 601 (2018). https://doi.org/10.1103/PhysRevFluids.3.062601

Nagata, R., Watanabe, T., Nagata, K.: Turbulent/non-turbulent interfaces in temporally evolving compressible planar jets. Phys. Fluids **30**(10), 105,109 (2018). https://doi.org/10.1063/1.5047395

Ohmichi, Y.: Preconditioned dynamic mode decomposition and mode selection algorithms for large datasets using incremental proper orthogonal decomposition. AIP Adv. **7**(7), 075,318 (2017). https://doi.org/10.1063/1.4996024

Pineau, P., Bogey, C.: Temperature effects on convection speed and steepened waves of temporally developing supersonic jets. AIAA J. **58**(3), 1227–1239 (2020). https://doi.org/10.2514/1.J058589

Rogers, M.M., Moser, R.D.: Direct simulation of a self-similar turbulent mixing layer. Phys. Fluids **6**(2), 903–923 (1994). https://doi.org/10.1063/1.868325

Rowley, C.W., Mezić, I., Bagheri, S., et al.: Spectral analysis of nonlinear flows. J. Fluid Mech. **641**, 115–127 (2009). https://doi.org/10.1017/S0022112009992059

Samie, M., Lavoie, P., Pollard, A.: Quantifying eddy structures and very-large-scale motions in turbulent round jets. J. Fluid Mech. **916**, A2 (2021). https://doi.org/10.1017/jfm.2021.183

Samie, M., Aparece-Scutariu, V., Lavoie, P., et al.: Three-dimensional large-scale and very-large-scale coherent structures in a turbulent axisymmetric jet. Journal of Fluid Mechanics **948**(September), (2022). https://doi.org/10.1017/jfm.2022.703

Schmid, P.J.: Dynamic mode decomposition of numerical and experimental data. J. Fluid Mech. **656**, 5–28 (2010). https://doi.org/10.1017/S0022112010001217

Schmid, P.J.: Dynamic mode decomposition and its variants. Annu. Rev. Fluid Mech. **54**(1), 225–254 (2022). https://doi.org/10.1146/annurev-fluid-030121-015835

Shamooni, A., Cuoci, A., Faravelli, T., et al.: An a priori dns analysis of scale similarity based combustion models for les of non-premixed jet flames. Flow Turbul. Combust. **104**(2), 605–624 (2020). https://doi.org/10.1007/s10494-019-00099-9

Sirovich, L.: Turbulence and the dynamics of coherent structures part ii: Symmetries and transformations. Q. Appl. Math. **45**(3), 573–582 (1987)

Taveira, R.R., da Silva, C.B.: Kinetic energy budgets near the turbulent/nonturbulent interface in jets. Phys. Fluids **25**(1), 015,114 (2013). https://doi.org/10.1063/1.4776780

Towne, A., Schmidt, O.T., Colonius, T.: Spectral proper orthogonal decomposition and its relationship to dynamic mode decomposition and resolvent analysis. J. Fluid Mech. **847**, 821–867 (2018). https://doi.org/10.1017/jfm.2018.283

Tso, J., Hussain, F.: Organized motions in a fully developed turbulent axisymmetric jet. J. Fluid Mech. **203**, 425–448 (1989). https://doi.org/10.1017/S0022112089001539

van Reeuwijk, M., Holzner, M.: The turbulence boundary of a temporal jet. J. Fluid Mech. **739**, 254–275 (2014). https://doi.org/10.1017/jfm.2013.613

Vuorinen, V., Keskinen, K.: Dnslab: A gateway to turbulent flow simulation in matlab. Comput. Phys. Commun. **203**, 278–289 (2016). https://doi.org/10.1016/j.cpc.2016.02.023

Watanabe, T., Nagata, K.: Integral invariants and decay of temporally developing grid turbulence. Phys. Fluids **30**(10), 105,111 (2018). https://doi.org/10.1063/1.5045589

Watanabe, T., Zhang, X., Nagata, K.: Direct numerical simulation of incompressible turbulent boundary layers and planar jets at high reynolds numbers initialized with implicit large eddy simulation. Comput. Fluids **194**(104), 314 (2019). https://doi.org/10.1016/j.compfluid.2019.104314

Xu, G., Antonia, R.A.: Effect of different initial conditions on a turbulent round free jet. Exp. Fluids **33**(5), 677–683 (2002). https://doi.org/10.1007/s00348-002-0523-7

Yang, Y., Wang, H., Pope, S.B., et al.: Large-eddy simulation/probability density function modeling of a non-premixed co/h2 temporally evolving jet flame. Proc. Combust. Inst. **34**(1), 1241–1249 (2013). https://doi.org/10.1016/j.proci.2012.08.015

Yule, A.J.: Large-scale structure in the mixing layer of a round jet. J. Fluid Mech. **89**(3), 413–432 (1978). https://doi.org/10.1017/S0022112078002670